processes

MDPI

Article

Quantitative Characteristics of Micro Bedding Fractures in the Wufeng–Longmaxi Formation Based on High-Resolution Map Imaging Technology

Conghui Zhao [1,*], Dong Wu [2], Fengbo Hu [1], Meng Sun [3], Tao Li [4] and Hu Wang [1,4,*]

[1] No. 1 Mud Logging Company of Bohai Drilling Engineering Company Ltd., CNPC, Tianjin 300280, China
[2] Information Center, Engineering Technology R&D Company Limited, CNPC, Beijing 102206, China
[3] Exploration and Development Research Institute of Huabei Oilfield Company, CNPC, Renqiu 062550, China; yjy_sm@petrochina.com.cn
[4] School of Earth Resources, China University of Geosciences (Wuhan), Wuhan 100083, China; litao826@cug.edu.cn
* Correspondence: zconghui@cnpc.com.cn (C.Z.); wanghu19@cug.edu.cn (H.W.)

Abstract: The study of microfractures in shale is mainly based on qualitative description. Conversely, quantitative description of the parameters of shale microfractures can provide a quantitative basis for shale fracture characterization and shale physical properties. Nine shale reservoir samples of the Wufeng–Longmaxi Formation in the Jiaoshiba area were studied, using the backscattered two-dimensional multiscale resolution imaging technology, combined with high-resolution map imaging technology (MAPS), and thousands of images were obtained using scanning electron microscopy. Gray image analysis was used to extract microfracture information from images (2 × 2 cm multiresolution). The "maximum circle method" was used to calculate the length and aperture characteristics of the fractures. Parameters such as the area of the bedding fractures, the surface rate of the fractures, and the linear density of the fractures were obtained by the integration of apertures. The fracture length was between 2~7 mm, the aperture was between 1~6 μm, the linear density was between 1~6/m and the surface rate was 1%. The bedding fractures do not contribute much to the porosity of the shale reservoir; however, shale reservoirs with high porosity have a high development of bedding fractures and good permeability. The development of a bedding fracture is controlled by the lithology within shale reservoirs. Different types of lithology contain different bedding fractures, but they have a certain regularity. Moreover, the content of organic matter and TOC (total organic content) in the shale reservoir control the development of a bedding fracture, where a high organic and TOC content are accompanied by a high number of fractures.

Keywords: shale; fracture length; aperture; line density of fracture; Sichuan basin

Citation: Zhao, C.; Wu, D.; Hu, F.; Sun, M.; Li, T.; Wang, H. Quantitative Characteristics of Micro Bedding Fractures in the Wufeng–Longmaxi Formation Based on High-Resolution Map Imaging Technology. *Processes* **2023**, *11*, 1942. https://doi.org/10.3390/pr11071942

Academic Editor: Junqian Li

Received: 22 May 2023
Revised: 19 June 2023
Accepted: 21 June 2023
Published: 27 June 2023

1. Introduction

With the increasing focus on the stimulation of reservoirs with low matrix permeability, the flow law of underground fluids in a natural fracture network and matrix pores, and the interaction between fluids and natural fractures, have become important factors in the study of underground aquifers and reservoirs [1].The development degree and distribution pattern of fractures are important geological parameters to analyze low permeability reservoirs [2]. Fractures of various scales are regarded as primary storage spaces in fractured shale oil reservoirs [3]. Natural fractures always serve as important seepage channels and storage spaces, which control the accumulation and preservation of shale gas [4]. The geometry of natural fracture systems and their effect on seepage is difficult to understand because of the limited availability of precise data from subsurface fracture systems.

Conventional 3D seismic data do not have sufficient resolution to capture fault systems, and other advanced microseismic techniques have limitations. Drilling data (e.g.,

directional core, image logging, mud loss) can provide detailed characteristic parameters of effective fractures in the reservoir. However, logging and cores can only provide one-dimensional fracture characteristics, and the orientation of fractures is not easy to determine. Meanwhile, the well spacing is generally too large, so it is difficult to analyze natural fractures between wells [5]. Outcrops can be used to study the spatial properties of 2D fracture systems [6,7]. Advances in digital outcrop modeling techniques, such as light detection and ranging and the use of unmanned aerial vehicles, allow three-dimensional mapping of outcrop fracture systems to be built, which could help to capture the full spatial distribution of fracture characteristics, including length and height distributions [8]. However, fracture apertures cannot be accurately obtained from outcrops due to weathering and denudation. Predicting the distribution of fractures in reservoirs based on geomechanical models is a commonly used method. Under the condition of in situ stress, it is completely feasible to use mechanical methods to predict fractures [9,10]. Among these methods, fracture density, orientation and length data can be obtained more accurately from outcrop data. However, the aperture parameter needs to be corrected by dynamic data [9]. Previous researches believed that the vertical stress will change and form bedding fractures after structural uplift and pressure relief, which are of positive significance to the development of shale reservoirs [11]. Through the observation of the fractures under the microscope and the statistical analysis of the fractures in the lab, the scanning electron microscope shows that the aperture of the microfractures is hundreds of nanometers to several microns, and the fractures with an aperture of less than 1 μm are defined as microfractures [12]. Gale et al. found that the aperture of natural microfractures is generally less than 50 μm in their study of fractures in the Barnett shale [1].

Compared with other methods, MAPS can ensure that the fracture aperture value can be fully extracted in a larger field of view (Figure 1). The MAPS technology is widely used in various industries [13–16]. In petroleum geology, it can qualitatively and quantitatively describe the rock micro skeleton and pore structure. Since the revolution of tight sandstone and shale oil in the United States, the contradiction between the microstructure and the size of the field of view has led to the birth of the MAPS technology, which is now successfully applied to the evaluation of the pore structure of tight sandstone and shale [17,18]. This study is mainly based on the MAPS method to collect image features of 2 × 2 cm shale reservoirs, and uses image analysis technology to count the length, aperture and density of the shale bedding fractures; it discusses the correlation between the bedding parameters, and the influence of bedding fractures on physical properties and controlling factors.

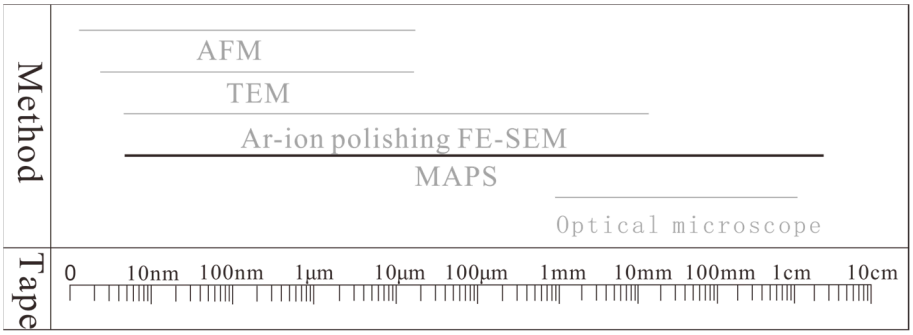

Figure 1. Scale diagram of image analysis method.

2. Samples and Experiment Methods

2.1. Geological Setting and Samples

The Fuling Shale Gas Field is located in the southeastern Sichuan Basin, which is tectonically located on the East Sichuan Barrier Fold Belt in the eastern segment of the Sichuan Basin [19]. The sampled well is located in the southeastern Fuling area, southeast of Chongqing City (Figure 2). The study area has undergone multiple episodes of tectonic uplift and subsidence [20]. During the Late Ordovician, a low-energy, under-compensation

and anoxia sedimentary environment was widespread [21,22]. At the end of the Ordovician and the beginning of the Silurian, global transgressions occurred twice and helped develop the Longmaxi organic-rich shale. The sedimentary environment of the Silurian Longmaxi Formation in the Fuling Shale Gas Field was a deep-water shelf [23]. The average thickness of gas-bearing shale is 89 m with stable distribution; the average organic matter abundance is 2.54%, and the average vitrinite reflectance is 2.5%; the average porosity is 4.61%, dominated by nanoscale mesopores [24,25]; the average content of brittle minerals is 56.53%; the Jiaoshiba block of the Fuling shale gas field has a gentle structure (formation dip angle 5~10°), without huge fractures, moderately buried (2250~3500 m) microfracture development; gas content 2~6 cubic meters/ton [26]. Among them, the average thickness of high-quality shale gas layer is 40 m in lower member, the average organic matter abundance is 3.03%, the average porosity is 4.8%, and the average gas content is 5~6 cubic meters/ton. It is an organic-rich and gas-rich shale section. The gas reservoir types are medium-deep, abnormally high pressure, dry gas and shale gas reservoirs [19,24].

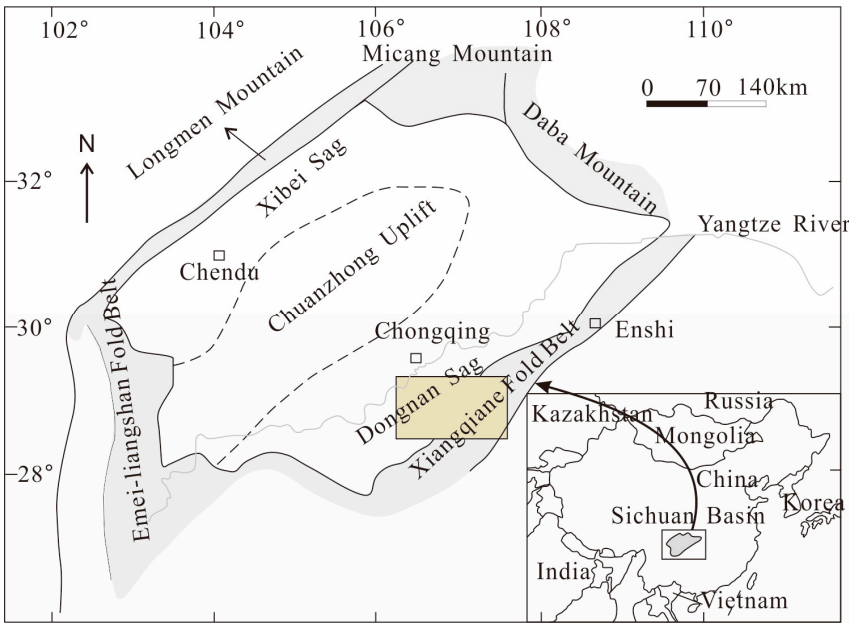

Figure 2. Location and structural zoning of the research area.

Nine shale samples from Wufeng–Longmaxi Formation were selected in the study area for scanning electron microscopy and image processing analysis (Figure 3). Relevant experimental methods and conclusions can be applied to the evaluation of shale microfractures in other shale gas fields around the world.

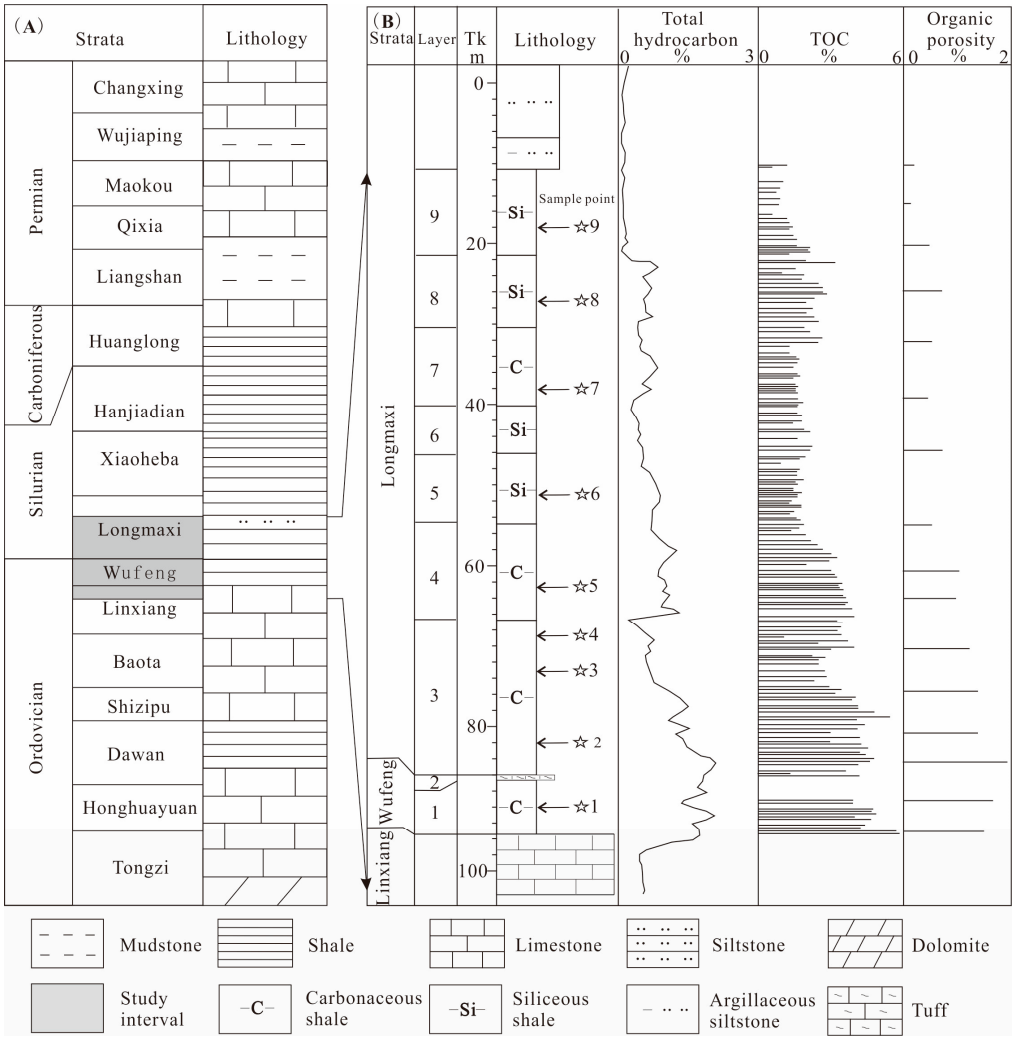

Figure 3. Lithological profile and sampling point location. (**A**) Stratigraphic sequence, lithology in the southeast of the Sichuan Basin and study interval. (**B**) Lithology, total hydrocarbon content, total organic matter content, and organic pore size of the Wufeng-Longmaxi Formation.

2.2. Experiment Methods

The experiment is divided into three parts: experimental sample preparation, experimental methods and image processing and analysis. The bedding of shale samples is well-developed, resulting in the preparation of experimental samples being very difficult. Ordinary rock sample cutting will cause a large amount of peeling off the bedding surface and destroy the samples. High-precision instruments must be used in the process of sampling and sample preparation. Because of the multiscale nature of microfractures, image acquisition and analysis must also be scientifically sound.

2.2.1. Sample Preparation

According to the results of the water immersion experiment, nine positions with different bubbling intensities were selected on the whole core, and the whole core drilling prototype was used. The rock samples were cylinders with 2.5 cm in diameter and 3~5 cm in length. The Iso Met 5000 precision cutting machine was used for end trimming and fine cutting to ensure that the two end faces were even, and to obtain thin slices with a diameter of about 25 mm and a thickness of 8 to 10 mm. Then the samples went through glue injection, grinding and polishing, to ensure that there was no pollutant on the polished surface before proceeding to the next step; then select the reverse direction of head and base when polishing; make a record. Using the Model 1060 Argon Ion Polisher, the surface

was polished by ion sputtering by ionizing the inert gas argon. In order to increase the conductivity of the sample surface, a layer of carbon film was sputtered on the sample surface by using ETD-100AF carbon-coating instrument.

2.2.2. Methods

(1) Two-dimensional multiscale resolution imaging of backscattering

The testing equipment used is Helios Nano Lab 660. Before the experiment, the sample chamber is checked to make the internal gas pressure equal to the external pressure. Open the door of the sample hatch, fix the prepared sample on the sample stage with carbon conductive tape, put the fixed sample into the sample chamber of the instrument, use the camera system to take a picture of it to navigate the sample stage, and then vacuumize the sample chamber. Select suitable area to be scanned under the appropriate voltage and beam current before turning on the electron beam. Generally, the voltage at start-up is 2 kV, and the beam current is 6.3 pA. Use the navigation interface to double-click the area to be scanned in the sample to the center and turn on the electron beam. After capturing scanned image at an appropriate magnification, perform operations such as focusing on it, automatically adjusting brightness and contrast, and eliminating astigmatism to make the image clear, so that the Z-axis of the sample stage coincides with the working distance WD. For higher image resolution, the sample stage was raised up to shorten the working distance. Continue to focus on the image in the area of interest, it can automatically adjust the brightness and contrast, eliminate astigmatism and other operations to make the image clear. Properly change the voltage and beam current to achieve the best image effect, and increase the scanning time after the image is clear to make the image clearer. Images are stored after scanning.

(2) High-Resolution Map Imaging

The test instrument used is Helios NanoLab 660. The high-resolution map imaging in large-area multilevel resolution images was made up of thousands of images obtained by scanning electron microscopy in map software. The images can be arbitrarily enlarged or reduced such as in Google Maps. It helps to understand the distribution area of the natural fine pores of the rock skeleton, the shape and distribution of fractures in a two-dimensional plane. Set the scanning area in the Maps software. The size of each scanned image, the number of scanned sheets, the scanning time, the image resolution, the overlapping range of the images and the automatic image collection are operated in proper order. After collecting all the images, use the Maps software to stitch them together. After stitching, use the HD View software to view the stitched large-scale images.

(3) Statistical method for quantitative characteristics of microfractures

Based on the MAPS scanning image, the image information of the effective fracture segment was captured (Figure 4A); the image was processed in grayscale using MATLAB 2022 software, and the effective microfracture information of the shale reservoir in the image was extracted (continuous blank part) (Figure 4B); the image accuracy is 250 nm represented by the size of each square being 250 nm × 250 nm, with d = 10 nm as the sampling interval, and the largest circle is made every distance d, and the diameter of the circle is the microfracture aperture at the sampling point. Connect all the centers of circles into a line, and the length of the line is the length of the microfracture (Figure 4C,D); the area of microfractures can be obtained.

$$S = \int_{0 \to D} R\mathrm{d}x \tag{1}$$

S is microfracture area, mm^2; D is total length of microfractures, mm; R is circle radius, mm; dx is sampling interval, mm.

$$\mathrm{P} = \mathrm{S}/\mathrm{Sy} \tag{2}$$

P is microfracture porosity, %; Sy is the area of sample image area, mm^2.

$$m = n/L \quad (3)$$

m is microfracture line density, /cm; n is the number of microfractures in the sample image; L is sample image side length, cm.

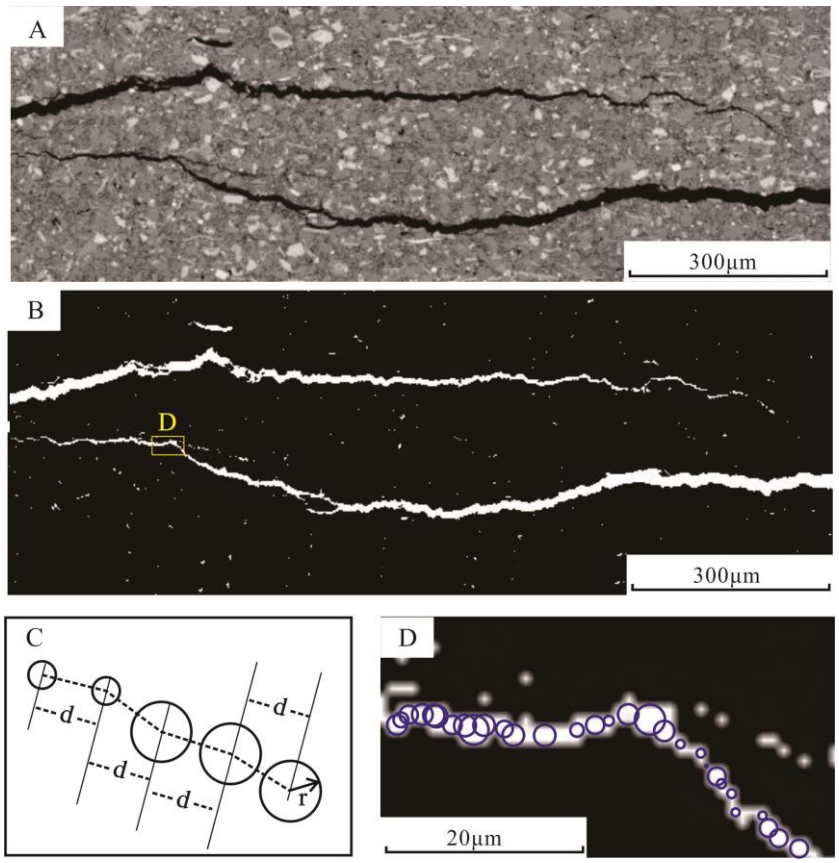

Figure 4. Measurement of fracture length and aperture by maximum circle method. (**A**) Scanning electron microscope image of the original fracture; (**B**) image after gray adjustment processing, extracting microfracture information; (**C**) schematic diagram of microfracture aperture measurement; (**D**) partial enlarged view of microfractures by integrating the statistics of fracture apertures (Formula (1)), which can be divided by the entire image area to obtain the surface porosity of microfractures (Formula (2)); the fracture line density can be obtained by dividing the number of statistical fractures by the image length (Formula (3)).

3. Results

The scanning resolution of microfractures in shale reservoirs is 250 nm. A total of 64 microfractures were found in the nine shale reservoir samples, 12 of which were considered to be artificial fractures formed during the later sample preparation, and the rest were mainly natural bedding fractures (Figure 5A,B). One end of some ply bedding fractures opened at the edge of the sample, and the effective length of the microfractures could not be counted in 15 pieces. Thus, only the parameters of the microfractures whose sealing positions at both ends were inside the sample were counted (Figure 5C,D). Therefore, there are 37 effective bedding fractures in the final statistics.

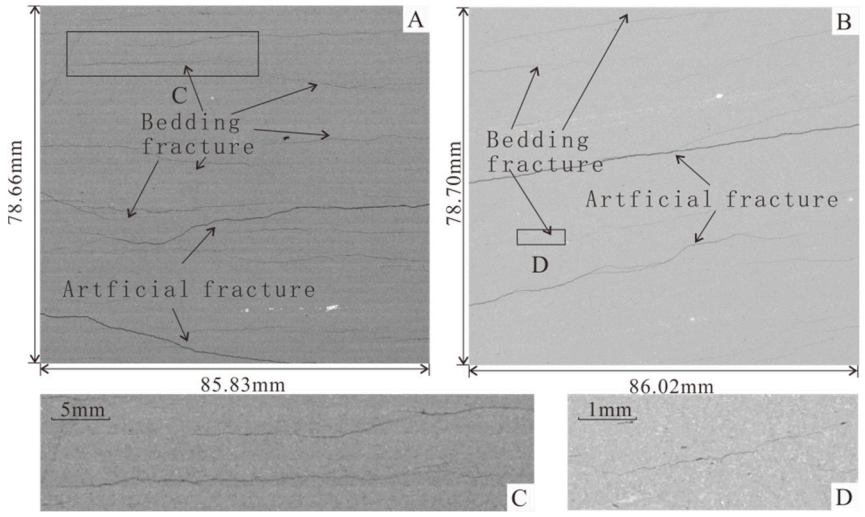

Figure 5. Fracture types within MAPS image. (**A**) 85.83 mm × 78.66 mm field of view image. (**B**) 86.02 mm × 78.70 mm field of view image, (**C**) Enlarged rectangular box from (**A**). (**D**) Enlarged rectangular box from (**B**).

3.1. Bedding Fracture Length

The lengths of the bedding fractures were between 0 and 11 mm, and the overall distribution was relatively uniform. The longest microfracture reached 20.84 mm, and the shortest was only 0.071 mm. The lengths of fractures were mainly concentrated in the 2~7 mm range, accounting for 0.6 of the total number of bedding fractures; fractures less than 1 μm in length accounted for 0.07 of the total number of bedding fractures; and fractures larger than 11 mm accounted for 0.10 of the total number of bedding fractures (Figure 6).

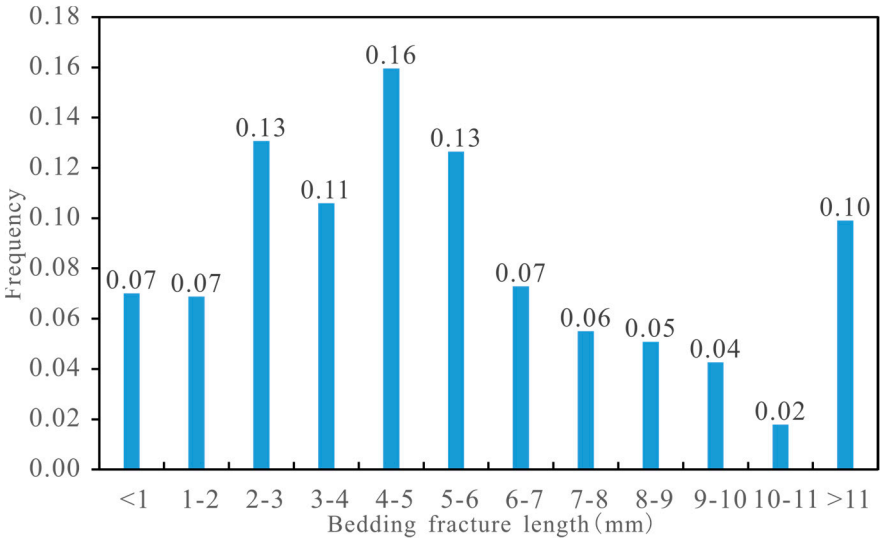

Figure 6. Frequency distribution of bedding fracture lengths.

3.2. Bedding Fracture Aperture

The degree of aperture has different definitions under different conditions. In this study, the natural fractures opened by natural stress were studied (Marrett et al., 1999). The apertures of the bedding fracture were between 0 and 11 μm, and the overall distribution was uneven. The bedding fracture with the largest aperture reached 61.20 μm, and the shortest was only 0.69 μm. Fracture lengths were mainly concentrated in 1~6 μm range, accounting for 0.84 of the total number of bedding fractures; fractures less than 1 μm

accounted for 0.03 of the total number of bedding fractures; and microfractures larger than 11 μm accounted for 0.02 of the total number of bedding fractures (Figure 7).

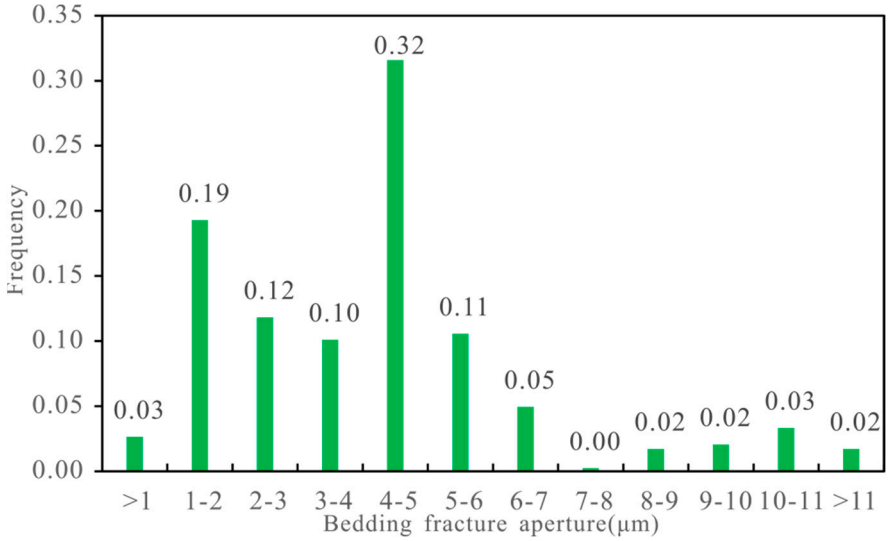

Figure 7. Frequency distribution of bedding fracture apertures.

3.3. Porosity and Linear Density of Bedding Fractures

Through observation and statistics under a microscope, software and manual methods were used to calculate the porosities and linear densities of bedding fractures. The surface rate of the bedding fracture was between 0.004~2.873%, with an extremely uneven distribution. The bedding fracture with the largest surface porosity reached 2.873%, and the minimum was 0.004%. The bedding fractures were mainly concentrated below 0.01%. The linear densities of bedding fractures were in the range of 120~606 pieces per meter, and the overall distribution was even. They were mainly concentrated in 1 to 3 pieces/cm (Table 1).

Table 1. Statistics of linear density and surface rate parameters (under the microscope).

Number	9	8	7	6	5	4	3	2	1
Surface rate (%)	0.011	0.012	0.061	2.873	0.878	0.005	0.005	0.004	0.006
Linear density (number/m)	606	343	321	288	287	246	177	184	120

The core observation results show that there is a significant vertical difference in the development degree of shale bedding fractures in the Wufeng–Longmaxi Formation, so the statistics are divided into sublayers. Overall, the development level of bedding fractures in the three small layers is the highest, with bedding fractures of up to 1813.5 pieces/m; the segment with the lowest development level is the ninth sublayer, with 368.9 pieces/m; the development degree of interlayer and foliation fractures in the Wufeng Formation shale reservoir is not high, with 877.9 pieces/m. The development degree of nonstructural fractures in the shale reservoir of the Longmaxi Formation gradually decreases from bottom to top (Figure 8), which is consistent with the actual production situation where the bottom gas layer is good and the top gas layer is poor. It is speculated that nonstructural fractures may be an important influencing factor on the gas production capacity of the gas field.

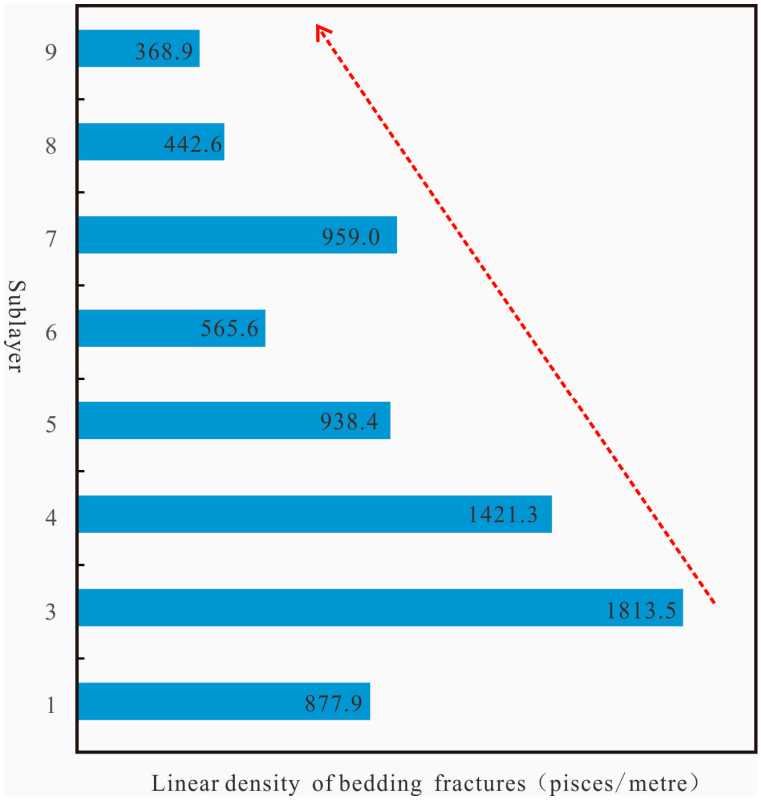

Figure 8. Longitudinal distribution characteristics of nonstructural fractures (core).

In summary, the longest nonstructural fracture was 20.84 mm, and the shortest was only 0.071 mm. The average opening of bedding fractures was 5 mm. Indoor experimental statistics show that the openings of bedding fractures ranged from 0 to 61.2 μm. These were mainly concentrated in the 1~6 μm range, with a mean of 5.4 μm. The development degree of bedding fractures in the third small layer was the highest, with a minimum of 1813.5 bedding fractures/m. The segment with the lowest development level was the ninth sublayer, with a minimum of 368.9 bedding fractures/m. The development degree of bedding fractures in the Wufeng Formation shale reservoir was not high, with 877.9 bedding fractures per meter.

4. Discussion

4.1. The Relationship between the Aperture and the Length of the Bedding Fracture

There is generally a power function relationship between the outcrop statistical fracture aperture and fracture frequency [27–29]. However, this geometric characteristic of fracture apertures has not taken into account the influence of fracture orientation and regional stress field disturbance caused by adjacent fractures [30]. Thin section data can help identify open fractures and quantitatively identify corresponding fracture apertures [31]. Normally,, whether it is a fracture caused by sedimentation or a fracture formed by later stress, there should be a quantitative relationship between the aperture of the fracture and the length of the fracture. According to the statistics regarding actual images, there is a positive correlation between the length of the bedding fracture and the aperture, which means longer bedding could form larger apertures (Figure 8). However, whether this relationship can be extended to larger-scale fracture features requires further practice and analysis data to supplement and improve the findings. It is also possible that there is a polynomial correlation between the two, within a certain scale range; the two are positively correlated, and when the fracture length reaches a certain level, its aperture will reach a peak (Figure 9). Due to scale effects, small changes in the opening and length of small-scale fractures can cause significant deviation. During the sample preparation process, issues such as the

magnitude of external forces, the angle of cutting through fractures and the angle of the sample itself can all cause deviations in the correlation between the fracture aperture and length.

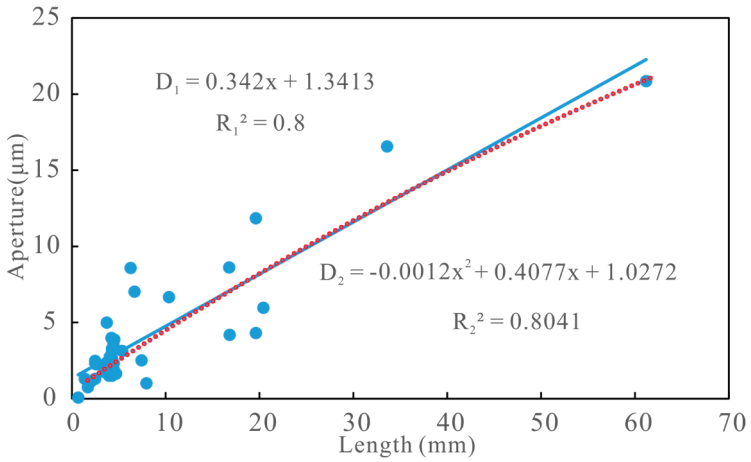

Figure 9. Relationship between aperture and length.

4.2. Influence of Bedding Fracture on Physical Properties

Due to the overlying pressure, the bedding fractures might be closed in the underground state, and the large-diameter pores and fractures are conducive to the accumulation and migration of oil and gas, which can effectively improve the physical properties of shale reservoirs [30,32]. The linear density of fractures and surface porosity data of shale reservoirs obtained by statistics from images were linearly regressed with the experimentally measured porosity data, and the correlation between surface porosity and reservoir porosity was shown to be poor (Figure 10). The density of the bedding fracture in the shale reservoir is obviously in positive correlation with porosity, and the correlation is good (Figure 10). The surface porosity accounts for about 1% of the actual porosity, and only a few data surface porosity values account for more than 50% of the total porosity (Table 2). The inspection found that there is a problem with these data: the opening of fractures may be caused by artificial sample preparation in the later stage. It shows that the linear density of shale fractures has little effect on the overall porosity of shale reservoirs, but the linear density of shale fractures in shale reservoirs with good porosity is high. The main effect of shale fractures is to improve the permeability of shale reservoirs, while it has little effect on the porosity.

Table 2. Quantitative characterization data of bedding fractures.

Well	Depth m	Linear Density Stricp/cm	Surface Rate %	Porosity %	Ratio %
JY15	2892.76	6.057	0.011	6.352	0.173
JY15	2883.92	3.433	0.012	4.3325	0.277
JY15	2874.02	3.207	0.061	3.875	1.574
JY15	2869.73	2.882	2.873	4.966	57.853
JY15	2864.89	2.873	0.878	4.553	19.284
JY15	2859.96	2.464	0.005	3.587	0.139
JY15	2844.08	1.765	0.005	4.56	0.110
JY15	2840.91	1.843	0.004	3.65	0.110
JY15	2836.96	1.2	0.006	3.54	0.169

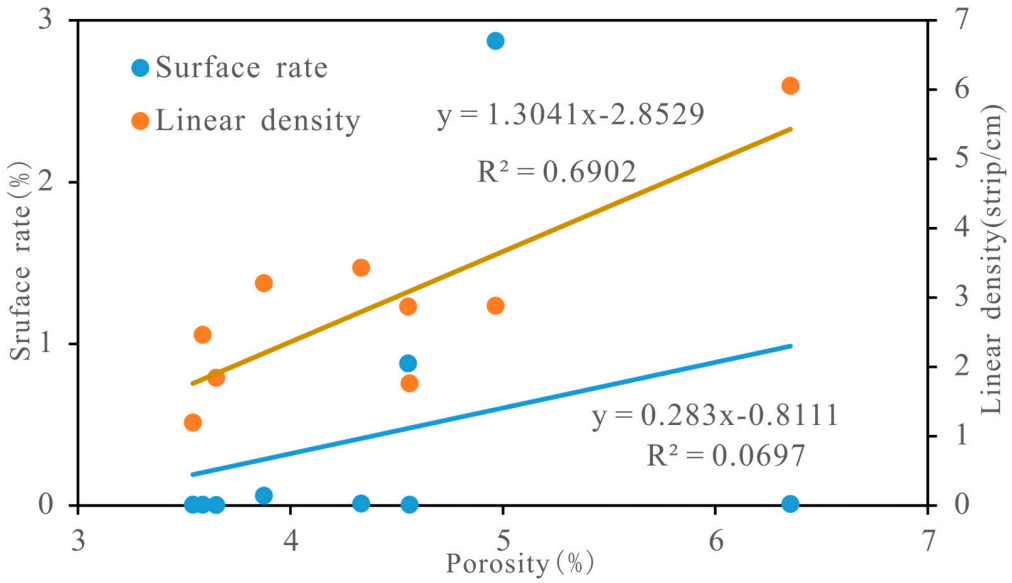

Figure 10. Correlation between surface rate, linear density and porosity.

4.3. Logging Prediction Method for Bedding Fractures

Previous researchers have conducted a lot of work on the main controlling factors of fracture development. Wang Ruyue and others believed that the development of fractures is mainly affected by multiple factors such as tectonic stress, structural location, organic matter content, mineral composition and content, lithology and rock mechanical properties, etc. [33,34]. At the same time, in order to meet the needs of drilling engineering, logging methods have been used for estimating quantification and three-dimensional direction [35]. For example, azimuth resistivity imaging logging has been increased with the lateral detection range to 2 m and the vertical resolution to 20 cm; and the vertical resolution of resistivity imaging logging has been improved to 5 mm, which can calculate the relative width or opening of fractures. The application of mathematical methods in logging can also improve the accuracy of fracture identification. The improvement in logging accuracy provides a theoretical basis for identifying fractures using logging methods.

Using the existing data and the GR value of the corresponding sampling point for data analysis, a positive correlation between the linear density of microfractures and GR was achieved (Figure 11). There may also be a correlation between the degree of development of microfractures and the lithology types of shale reservoirs. The development of microfractures may depend significantly on the lithology types of shale, which is in a certain regularity. Ou Chenghua et al. analyzed and discussed the fractures of shale with different lithologies, and established a three-dimensional discrete network model for shale reservoir lithofacies characterization and fractures [36]. That is because high GR values mean a high TOC and brittle minerals, which is conducive to the formation of shale bedding fractures. Therefore, the content of organic matter and TOC in shale reservoirs also controls the development degree of shale bedding fractures, and the parts with a high organic matter content have a high degree of development of shale fractures.

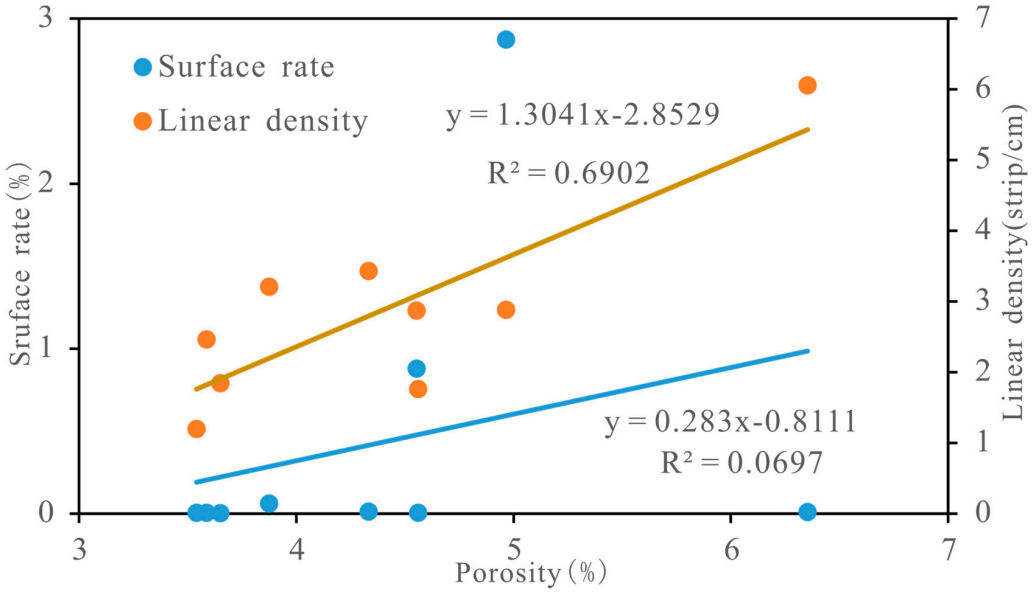

Figure 11. Correlation between linear density and GR correlation.

5. Conclusions

High-resolution map imaging (MAPS) technology was used to observe micron-scale fractures in shale reservoirs. The μm-scale fractures are important channels for fluid flow in shale reservoirs, which can communicate with the free or adsorbed shale gas in the agglomerated organic matter. The existence of bedding fractures also provides a rupture point for later fracturing.

The "maximum ball method" can be used to accurately calculate the quantitative characteristics of the length, aperture, surface porosity and linear density of the bedding fracture. The shale reservoirs in the Jiaoshiba area are mainly concentrated in the length of 2~7 mm, the aperture is between 1~6 μm, the linear density is 1~6 pieces/cm and the surface density is about 1%. There is no obvious correlation between the surface porosity of bedding fractures and porosity, which implies that the development degree of bedding fractures has little effect on shale porosity. However, an obvious positive correlation between the density of a bedding fracture and porosity indicates that where the degree of porosity is high, the development of bedding fractures is high, resulting in good physical properties and connectivity in the shale reservoir.

The development degree of bedding fractures is controlled by the lithology of shale reservoirs since the different shale lithologies developed different fractures. The content of organic matter in shale reservoirs also controls the development degree of shale bedding fractures, and the layers with high organic matter content have a high degree of development of bedding fractures.

The methods based on image analysis and recognition technology have universality in the same type of oil and gas reservoirs worldwide. Given the differences in geological conditions in different regions and the limitations in sample quantity, relevant quantitative conclusions can serve as a reference of magnitude when applied in different regions. The actual results should be based on the actual conclusions of the region.

Author Contributions: C.Z. and H.W., methodology; D.W., software; F.H., validation; M.S. and T.L., data curation. All authors have read and agreed to the published version of the manuscript.

Funding: This research is sponsored by the National Natural Science Foundation of China (No. 41202103, No. 41902127) and the China Postdoctoral Science Foundation (No. 2021M703000): Formation mechanism of compressive fracture network constrained by weak surface of shale bedding.

Data Availability Statement: All data has been presented in the manuscript.

Acknowledgments: We thank all anonymous reviewers for their constructive comments and suggestions.

Conflicts of Interest: We declare no conflict of interest.

References

1. Gale, J.F.W.; Reed, R.M.; Holder, J. Natural fractures in the Barnett Shale and their importance for hydraulic fracture treatments. *AAPG Bull.* **2007**, *91*, 603–622.
2. Ju, W.; Sun, W. Tectonic fractures in the Lower Cretaceous Xiagou Formation of Qingxi Oilfield, Jiuxi Basin, NW China Part one: Characteristics and controlling factors. *J. Pet. Sci. Eng.* **2016**, *146*, 617–625.
3. Fu, X.; Gong, L.; Su, X.; Liu, B.; Gao, S.; Yang, J.; Qin, X. Characteristics and Controlling Factors of Natural Fractures in Continental Tight-Oil Shale Reservoir. *Minerals* **2022**, *12*, 1616. [CrossRef]
4. Xu, X.; Zeng, L.; Tian, H.; Ling, K.; Che, S.; Yu, X.; Shu, Z.; Dong, S. Controlling factors of lamellation fractures in marine shales: A case study of the Fuling Area in Eastern Sichuan Basin, China. *J. Pet. Sci. Eng.* **2021**, *207*, 109091. [CrossRef]
5. Bisdom, K.; Gauthier, B.; Bertotti, G.; Hardebol, N. Calibrating discrete fracture-network models with a carbonate three-dimensional outcrop fracture network: Implications for naturally fractured reservoir modeling. *AAPG Bull.* **2014**, *98*, 1351–1376. [CrossRef]
6. Schultz, R.A.; Soliva, R.; Fossen, H.; Okubo, C.H.; Reeves, D.M. Dependence of displacement–length scaling relations for fractures and deformation bands on the volumetric changes across them. *J. Struct. Geol.* **2008**, *30*, 1405–1411. [CrossRef]
7. Zeeb, C.; Gomez-Rivas, E.; Bons, P.D.; Blum, P. Evaluation of Sampling Methods for Fracture Network Characterization Using Out-crops. *AAPG Bull.* **2013**, *31*, 291–295.
8. Reif, D.; Grasemann, B.; Faber, R. Quantitative Structural Analysis using Remote Sensing Data (Kurdistan, NE Iraq). *AAPG Bull.* **2011**, *95*, 941–956.
9. Bourne, S.J.; Rijkels, L.; Stephenson, B.J.; Willemse, E.J. *Predictive Modelling of Naturally Fractured Reservoirs Using Geomechanics and Flow Simulation*; Society of Petroleum Engineers: Abu Dhabi, United Arab Emirates, 2000.
10. Guiton, M.L.; Sassi, W.; Leroy, Y.M.; Gauthier, B.D. Mechanical constraints on the chronology of fracture activation in folded Devonian sandstone of the western Moroccan Anti-Atlas. *J. Struct. Geol.* **2003**, *25*, 1317–1330. [CrossRef]
11. He, Z.; Hu, Z.; Nie, H.; Li, S.; Xu, J. Characterization of shale gas enrichment in the Wufeng Formation–Longmaxi Formation in the Sichuan Basin of China and evaluation of its geological construction–transformation evolution sequence. *J. Nat. Gas Geosci.* **2017**, *2*, 724–733. [CrossRef]
12. Wang, J.; Zhu, Y.; Gong, Y.; Fang, H. Influential Factors and Forecast of Microfracture Development Degree of Longmaxi Formation Shales in Nanchuan Region, Chongqing. *Nat. Gas Geosci.* **2015**, *26*, 1579–1586.
13. Chen, Z.; Lenthe, W.; Stinville, J.C.; Echlin, M.; Pollock, T.M.; Daly, S. High-Resolution Deformation Mapping Across Large Fields of View Using Scanning Electron Microscopy and Digital Image Correlation. *Exp. Mech.* **2018**, *58*, 1407–1421. [CrossRef]
14. Kalinin, S.V.; Ophus, C.; Voyles, P.M.; Erni, R.; Kepaptsoglou, D.; Grillo, V.; Lupini, A.R.; Oxley, M.P.; Schwenker, E.; Chan, M.K.Y.; et al. Machine learning in scanning transmission electron microscopy. *Nat. Rev. Methods Prim.* **2022**, *2*, 11. [CrossRef]
15. Wang, H.; He, Z.; Zhang, Y.; Su, K.; Wang, R. Quantitative identification of microfractures in the marine shale reservoir of the Wufeng-Longmaxi Formation using water immersion tests and image characterization. *Interpretation* **2018**, *6*, SN23–SN30. [CrossRef]
16. Zheng, H.; Lu, X.; He, K. In situ transmission electron microscopy and artificial intelligence enabled data analytics for energy materials. *J. Energy Chem.* **2021**, *68*, 454–493. [CrossRef]
17. Li, W.; Lu, S.; Wang, M.; Zhou, N.; Cheng, Z. Quantitative characterization of micro heterogeneity of tight reservoirs by large-view FE-SEM Msplicing technology. *Oil Gas Geol.* **2022**, *43*, 1497–1504. [CrossRef]
18. Li, Z.; Zhao, S.; Feng, X.; Liu, Y.; Li, B.; Xia, Z.; Zhang, C.; Cao, L. Application of larbe field splicinb scanninb electron microscopy on quantitatively evaluation of shale pore structure: A case study of Lonbmaxi Formation reservoir in deep western Chongqing Block to southern Sichuan. *Pet. Reserv. Eval. Dev.* **2021**, *11*, 569–576.
19. Gao, D.; Duan, T.; Wang, Z.; Shang, X. Caledonian detachment deformation and deposition in the Fuling gas field of the southeastern Sichuan Basin in China: Implications for the Lower Silurian Longmaxi Shale gas exploration and production. *Interpretation* **2018**, *6*, SN119–SN132. [CrossRef]
20. Liu, R.; Hao, F.; Engelder, T.; Zhu, Z.; Yi, J.; Xu, S.; Teng, C. Influence of tectonic exhumation on porosity of Wufeng–Longmaxi shale in the Fuling gas field of the eastern Sichuan Basin, China. *AAPG Bull.* **2020**, *104*, 939–959. [CrossRef]
21. Wu, J.; Yuan, Y.; Niu, S.; Wei, X.; Yang, J. Multiscale characterization of pore structure and connectivity of Wufeng-Longmaxi shale in Sichuan Basin, China. *Mar. Pet. Geol.* **2020**, *120*, 104514. [CrossRef]
22. Zhang, Y.; He, Z.; Jiang, S.; Lu, S.; Xiao, D.; Chen, G.; Zhao, J. Factors Affecting Shale Gas Accumulation in Overmature Shales Case Study from Lower Cambrian Shale in Western Sichuan Basin, South China. *Energy Fuels* **2018**, *32*, 3003–3012. [CrossRef]
23. Wang, R.; Ding, W.; Gong, D.; Zeng, W.; Wang, X.; Zhou, X.; Li, A.; Xiao, Z. Development characteristics and major controlling factors of shale fractures in the Lower Cambrian Niutitang Formation, southeastern Chongqing-northern Guizhou area. *Acta Pet. Sin.* **2016**, *37*, 832. [CrossRef]
24. Wang, H.; He, Z.; Jiang, S.; Zhang, Y.; Nie, H.; Bao, H.; Li, Y. Genesis of Bedding Fractures in Ordovician to Silurian Marine Shale in Sichuan Basin. *Energies* **2022**, *15*, 7738. [CrossRef]

25. Yang, R.; He, S.; Hu, Q.; Hu, D.; Yi, J. Geochemical characteristics and origin of natural gas from Wufeng-Longmaxi shales of the Fuling gas field, Sichuan Basin (China). *Int. J. Coal Geol.* **2017**, *171*, 1–11. [CrossRef]
26. Ma, X.; Jun, X. The progress and prospects of shale gas exploration and development in southern Sichuan Basin, SW China. *Petrol. Explorat. Develop.* **2018**, *45*, 172–182. [CrossRef]
27. Hooker, J.N.; Gale, J.F.W.; Gomez, L.A.; Laubach, S.E.; Marrett, R.; Reed, R. Aperture-size scaling variations in a low-strain aperture-mode fracture set, Cozzette Sandstone, Colorado. *J. Struct. Geol.* **2009**, *31*, 707–718.
28. Hooker, J.N.; Laubach, S.; Marrett, R. A universal power-law scaling exponent for fracture apertures in sandstones. *Geol. Soc. Am. Bull.* **2014**, *126*, 1340–1362. [CrossRef]
29. Hooker, J.; Laubach, S.; Marrett, R. Fracture-aperture size—Frequency, spatial distribution, and growth processes in strata-bounded and non-strata-bounded fractures, Cambrian Mesón Group, NW Argentina. *J. Struct. Geol.* **2013**, *54*, 54–71. [CrossRef]
30. Alzayer, Y.; Eichhubl, P.; Laubach, S.E. Non-linear growth kinematics of aperture-mode fractures. *J. Struct. Geol.* **2015**, *74*, 31–44.
31. Liang, C.; Jiang, Z.; Cao, Y.; Wu, M.; Guo, L.; Zhang, C. Deep-water depositional mechanisms and significance for unconventional hydrocarbon exploration: A case study from the lower Silurian Longmaxi shale in the southeastern Sichuan Basin. *AAPG Bull.* **2016**, *100*, 773–794.
32. Li, Y.; Tang, D.; Wu, P.; Niu, X.; Wang, K.; Qiao, P.; Wang, Z. Continuous unconventional natural gas accumulations of Carboniferous-Permian coal-bearing strata in the Linxing area, northeastern Ordos basin, China. *J. Nat. Gas Sci. Eng.* **2016**, *36*, 314–327. [CrossRef]
33. Guo, X.; Hu, D.; Wei, X.; Li, Y. Main controlling factors on shale fractures and their influences on production capacity in Jiaoshiba area, the Sichuan Basin. *Oil Gas Geol.* **2016**, *37*, 799–808.
34. Zhu, T.; Wang, F.; Yu, L.; Sun, R. Controlling factors and types of shale gas enrichment in the Sichuan Basin. *Oil Gas Geol.* **2016**, *37*, 399–407.
35. Tang, X.; Li, S.; Xu, S.; Su, Y.; Zhuang, C. Acoustic Characterization and Imaging of Shale Gas Fractures in Horizontal Wells:Field Case Study in the Sichuan Basin of Southwest China. *Well Logging Technol.* **2017**, *41*, 501–505.
36. Ou, C.; Li, C. 3D discrete network modeling of shale bedding fractures based on lithofacies characterization. *Pet. Explor. Dev.* **2017**, *44*, 336–345. [CrossRef]